2

Near-Field Scanning Optical Microscopy Applied to the Study of Ferroelectric Materials

Josep Canet-Ferrer and Juan P. Martínez-Pastor
Institut de Ciència dels Materials de la Universitat de València. I(CM)UV
Spain

1. Introduction

During the last century, the spatial resolution of the optical microscope reached its theoretical limit which is given by diffraction of light and hence close to its wavelength (Abbe, 1882). As a result, several techniques like electron microscopy, tunnel effect or Scanning Probe Microscopy (SPM), were proposed as alternatives to improve spatial resolution. Despite several optical techniques are beating the diffraction limit (Hell & Stelzer, 1992; Harke et al., 2008) in general optical microscopy resolution is considerably limited at the fast growing field of Nanotechnology. In fact, the optimization of electro-optical devices sometimes requires the study of material properties below the nanometre scale. For that purpose, the resolution of the Transmission Electron Microscope (TEM) is the highest one being able to observe the atomic structure (and composition) of a vast number of compounds. The inconveniences of this powerful technique are related with the preparation of the material under study since the sample thickness must be reduced to 100 nm. Alternatively, the Scanning Electron Microscope (SEM) is often used for structural characterization when atomic resolution is not mandatory. The SEM is a valuable tool for imaging metallic or semiconductor samples, but it results less useful for characterizing dielectric materials. For this reason, Atomic Force Microscopy (AFM) could be considered the best option for studying ferroelectric surfaces. Other than morphology, the measurement of physical magnitudes can be also performed by means of the AFM (Asenjo et al., 2006; Cefali et al., 2003; Kwak et al., 2000), which leads to another important advantage with respect to electron microscopes. In fact, most of the experiments previously performed in different fields of Material Science have been revisited at the nanometer scale by means of advanced SPM techniques. Given the great variety of them, in this chapter we focus our attention in the Near-field Optical Scanning Microscope (NSOM), because of during last years it has been revealed as a powerful technique for studying ferroelectric domains and domain walls in a non-invasive way, (Eng & Gutherodt, 2000; Lamela et al., 2007, 2009; Lifante et al., 2008).

The AFM can be considered the simplest but also the most versatile scanning probe instrument, since most of the SPMs are developed on the basis of an AFM, as described in Section 2. The NSOM is one of these rather recent techniques, which allows the microscope user to study optical features and correlate with the topography that is being registered

simultaneously. Thanks to this fact, NSOM has been successfully used to characterize domain walls between inverted poled ferroelectric domains, to define the refractive index profiles of metal diffused channel waveguides or in order to identify solid phases embedded into ferroelectric layers (Canet-Ferrer et al., 2006a, 2006b, 2007, 2008). For a better understanding of the NSOM images, in Section 3 it is proposed a theoretical approach to explain some near-field effects typically observed on ferroelectric materials. Our formalism is based in the angular spectra decomposition of the near-field, which is considered to propagate into an effective dielectric constant media. Thanks to the magnitude of the optical contrast and geometry of the domain walls, using such a simple formalism we can obtain semi-quantitative information of the refractive index profile in ferroelectric materials. In section 4 we will show the experimental NSOM possibilities by means of the characterization of a well known ferroelectric surface: the potassium niobate (KNO). Finally, the experimental results are semi-quantitatively explained by means of the formalism described in section 3.

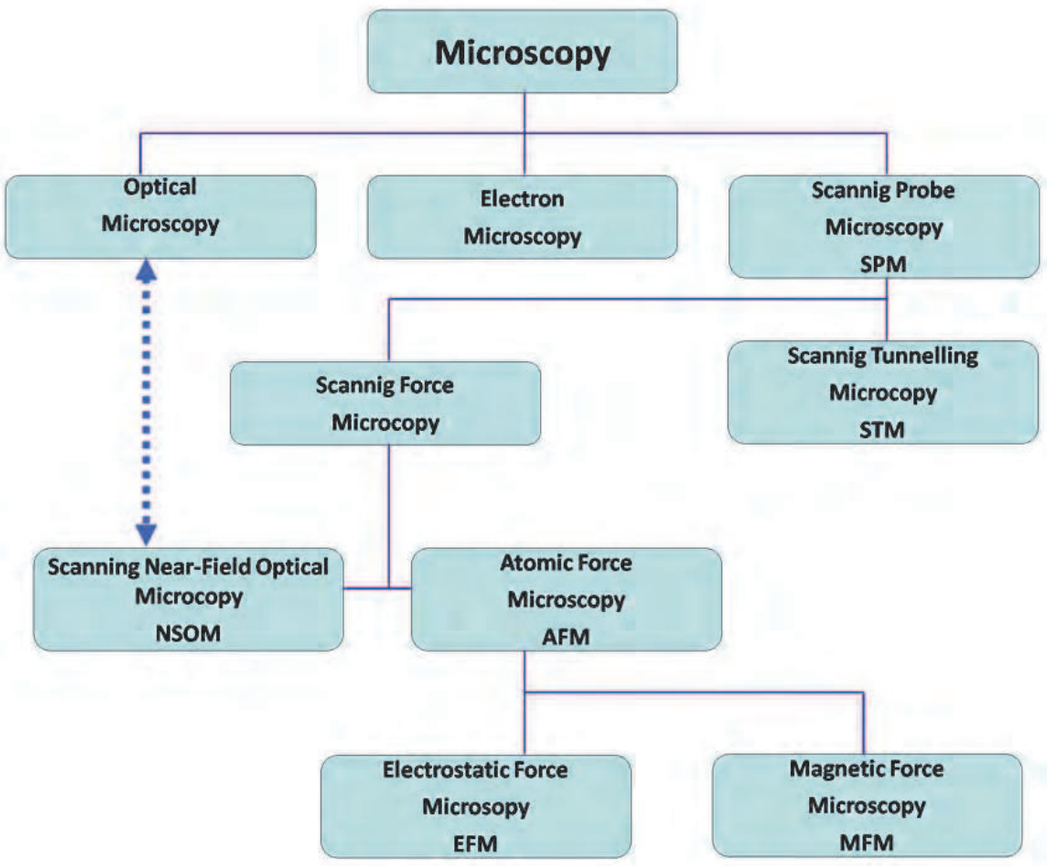

Fig. 1. Summary of the classification of new microscopes. The Scanning Probe Microscopy can be divided in tunnel and force-probe microscopes. The AFM is the most simple of the last ones but it is also the base of a vast number of advanced force microscopy techniques. The NSOM can be considered as a force-probe microscope being the main differences with the AFM related with the feedback system.

2. Experimental details of the AFM

This section consists of a brief introduction to the AFM technique followed by the description of the commercial electronics used by experimental set-up in this work. As a peculiarity, we can mention that the SPM techniques were proposed many years ago, but they could not be developed until the 80s because of such techniques required positioning systems of great precision. Nowadays, thanks to existence of piezoelectric positioners and scanners, the tip-sample distance can be controlled with a precision in the order of the Angstrom. As a result, the AFM resolution is limited by other effects different from relative tip-sample motion precision.

2.1 The AFM

The basis of the AFM is the control of the local interaction between the microscope probe and the material surface. The probe, usually a silicon nano-tip, is located at the end of a micro-cantilever. To obtain images of the sample topography, the distance between the tip and the sample is kept constant by an electric feedback loop. The AFM working principle varies depending on the operation mode. In the case of ferroelectric surfaces the most used method is the "non-contact mode" due to the fact that such mode allows the simultaneous measurement of electrostatic interactions (Eng et al., 1998, 1999). Working in non-contact mode, an external oscillation is induced to the cantilever by means of a mechanical actuator. In our commercial AFM (*Nanotec Electronica S.L.*) a Schäffer-Kirchoff® laser is mounted in the tip holder for monitoring the cantilever motion. The laser beam (<3mW at 659 nm wavelength) is aligned in order to be focused in the cantilever (see Fig. 2a) impinging the reflected light in a four-quadrant photodetector (Fig. 2b). In this way, the cantilever oscillation can be determined by comparison between the signals measured in the four diodes of the detector. If the frequency of the external excitation is close to the resonant frequency of the cantilever (i.e. 14-300 kHz), the oscillation amplitude generates an analogical signal that can be measured using lock-in techniques (synchronous amplification). Far away of the sample surface, the dynamics of the cantilever-tip system can be approached to a forced (driven) harmonic oscillator. But if the probe is located close to the sample (in the range of 10-25 nm), the tip is exposed to the surface interaction and the harmonic oscillator is damped by *van der Waals* forces. Since the damping force is determined by the position of the tip with respect to the sample, the oscillation amplitude also depends on such distance. For this reason, the feedback control maintains the oscillation amplitude in order to keep constant the tip-sample distance during the scan. Therefore, as the feedback correction consists in a displacement of the tip along the Z-axis, the sample roughness is reproduced by the tip motion which is monitored to obtain AFM topography images.

Nowadays, the AFM tip fabrication process has received much attention in order to obtain an enhancement of the microscope resolution, due to the fact that the tip size and shape determine the interaction forces. In addition, the tip can suffer other modifications like cobalt coating for MFM probes or doping for local current measurements. In this sense, several AFM advanced techniques can be performed using the appropriate tip in order to obtain electrostatic or magnetic information of the surface with an important resolution enhancement. We describe below the modifications introduced in our commercial AFM (electronics) for obtaining optical information of the sample surface.

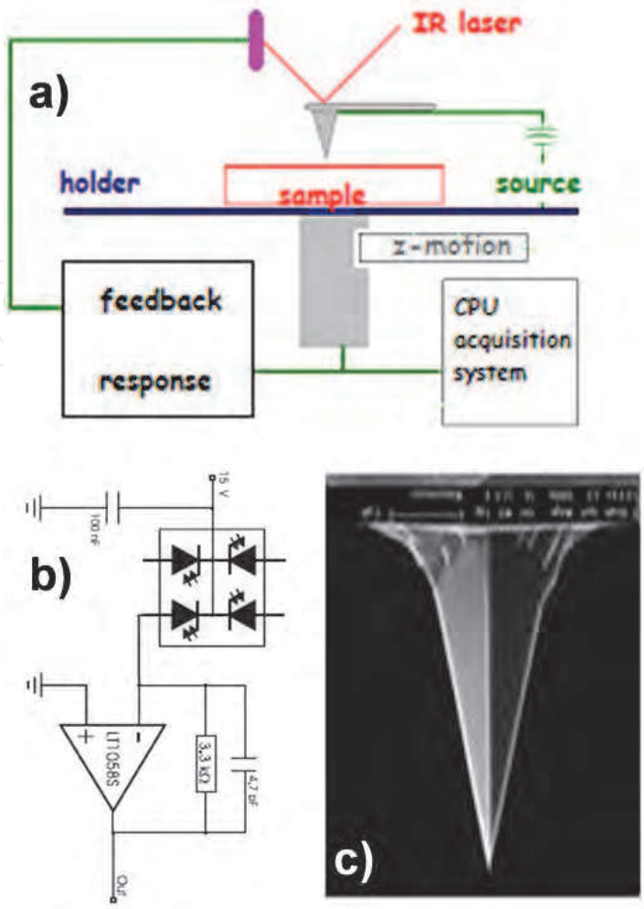

Fig. 2. (a) AFM scheme. (b) four-quadrant photodetector. (c) Standard Silicon probe (PointProbePlus, *Nanosensors*^{TM}).

2.2 The NSOM

The NSOM is a SPM technique whose resolution is limited by the probe parameters and which allows the microscope user to obtain the optical and the topography information simultaneously (Kawata, Ohtsu & Irie, 2000; Paeleser & Moyer, 1996). This fact makes NSOM a valuable tool in the study of materials at the nanometer scale by refractive index contrast, surface backscattering or light collection at local level.

Our NSOM is based on a tuning-fork sensor head, whose setup (Fig. 3a) is similar to that of a commercial AFM working in dynamic mode, but in this case, the standard silicon probe is replaced by a tip shaped optical fibre (Fig. 3b). The probe is mounted on a tuning pitch-fork quartz sensor (AttoNSOM-III from *Attocube Systems AG*), which is driven at one of its mechanical resonances, parallel to the sample surface Fig. 3c. In a similar way than at AFM, this vibration is kept constant by the AFM feedback electronics in order to maintain the tip-sample distance. The tuning fork sensor is controlled with the feedback electronics and data acquisition system used in our commercial AFM (Dulcinea from *Nanotec S.L.*). Simply the AFM tapping motion is substituted by the shear force oscillation of the tuning-fork quartz. Our NSOM is used in illumination configuration under a constant gap mode (Figure 3a) in order to obtain transmission images, by measuring the transmitted light using an extended

silicon photodetector located on the sample holder. For this purpose, the excitation light (laser diode) is delivered through a 2x2 fibre beam splitter using one of the coupler inputs (I1). One of the beam splitter outputs (O1) is connected to the fibre probe while the other output (O2) can be used to control the excitation power. Finally, the light reflected at the sample surface is guided to another photodetector thought the remaining beam splitter input (I2). The electrical signals (reflection and transmission) produced by both photodetectors are coupled to a low noise trans-impedance pre-amplifier and processed by the AFM image acquisition system (i.e. a digital sample processor). Even in previous works, the comparison of transmission and reflection images has been determinant for the understanding of the experimental results; in ferroelectric materials we are going to focus our attention on transmission images exciting the sample with 660nm wavelength.

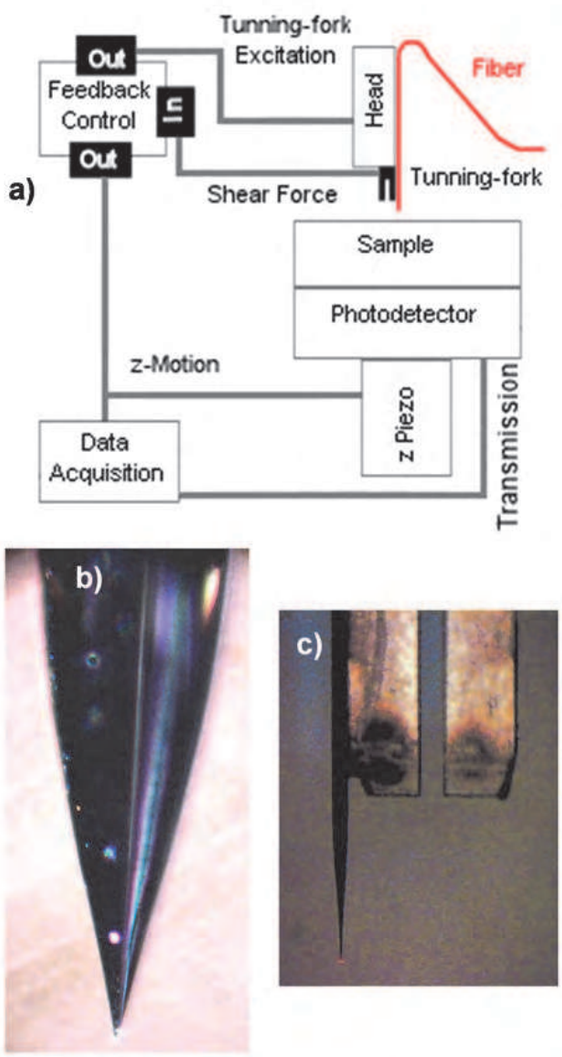

Fig. 3. (a) NSOM illumination scheme, pictured taken from (Canet-Ferrer et al., 2007). (b) NSOM probe prepared in our lab: aluminium coated tip. (c) The NSOM probe mounted on one of the arms of a tuning fork.

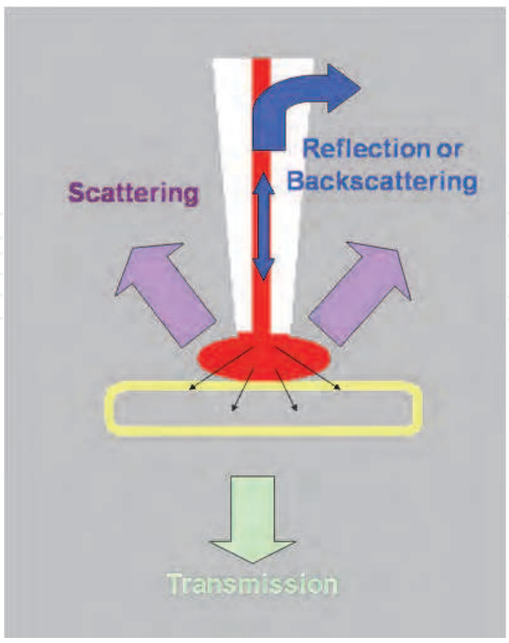

Fig. 4. Different kinds of near-field optical signals. All of them could be measured in illumination configuration.

3 Theoretical approach

3.1 2D model for NSOM optical transmission

Optical images acquired by NSOM can be treated by means of theoretical calculations in order to extract all the information they contain, but unfortunately, there is not a friendly analytical expression to describe transmitted signal under near-field conditions through a sample whose surface usually exhibits a random roughness. In this sense, the task of reproducing a refractive index profile of surface and sub-surface objects from optical transmission contrasts requires a great calculation effort to obtain accurate results. In addition, the surface characteristics of ferroelectric materials present other difficulties to perform quantitative analysis of the optical contrasts since some parameters are not exactly known, as the density of doping atoms, diffusion mechanism or strain maps. Fortunately, sometimes it is enough discriminating the domain structure for achieving valuable information for the optimization of the material applications. In this sense, NSOM transmission images can be easily interpreted if we take the next considerations in a 2D-model: (i) the sample is considered a flat surface composed by two different layers whose thicknesses would depend on the sample characteristics; (ii) an effective refractive index is considered at the upper-layer depending on the tip position (i.e. at each pixel of the image), while the second layer present an homogeneous refractive index; and (iii) the electromagnetic field distribution in the plane of the probe aperture is approached to a Gaussian spatial distribution with a standard deviation $\sigma \sim 80$ nm (i.e., approximately the tip aperture diameter), as illustrated in Fig. 5(a). Taking into account these considerations the light transmission contrasts can be simulated as follows.

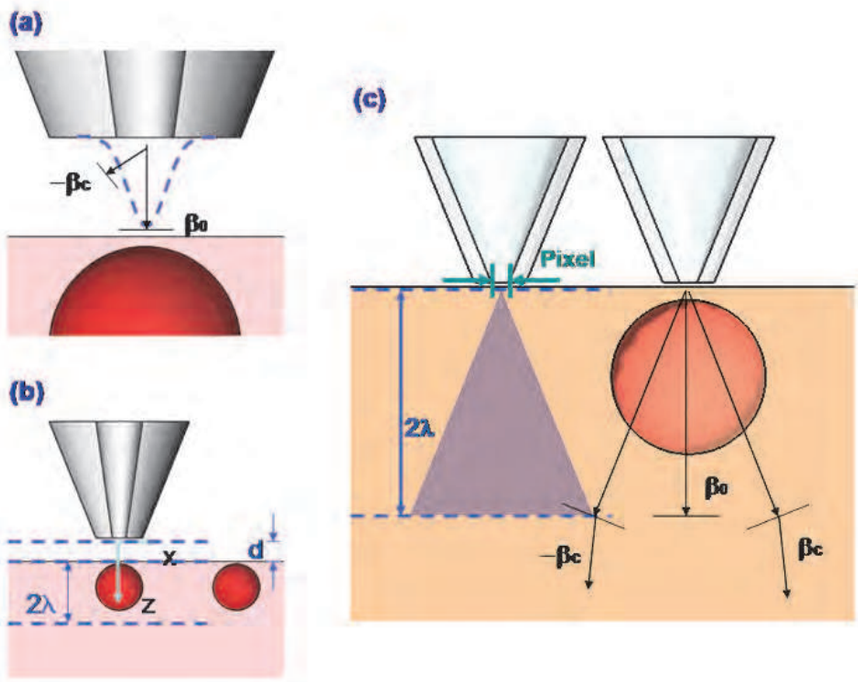

Fig. 5. (a) Near-field probe close to the feedback range. The optical intensity on the aperture plane is approached to a Gaussian field distribution. (b) Scheme of the main interfaces considered in our 2D simulation. Working at constant gap mode the tip is maintained at a distance, d, of a few nanometers. The upper layer is considered as a flat film (2λ thickness) with an average refractive index, $n_{eff}(x, y)$, which depends on the position. Below the channel upper-layer (at a far-field distance), we find the homogeneous media (the pictures are not at a correct scale in all dimensions). (c) 2D representation of the near-field probe (80 nm) in feedback range close to a scatter object larger than the wavelength. The relative position of the propagating light cone and the sphere immersed in the upper layer depends on their optical convolution. Therefore, a different effective refractive index n_{eff} is expected for each pixel of the NSOM tip scan. Figure taken from (Canet-Ferrer et al., 2008).

Firstly, the electromagnetic field distribution coming from the optical probe is decomposed into its angular spectrum.

$$E(x, z=0) = \sum_{\beta=-\pi/2}^{\beta=\pi/2} c^{(\beta)} e^{k_x x} \tag{1}$$

The excitation light is developed into a linear combination of plane-waves simplifying the calculations since the transmission for each component can be treated separately (Nieto-Vesperinas, 2006). Such decomposition consists of a 2D-Fourier transform of the propagating and evanescent plane waves:

$$c^{(\beta)} = \sigma\sqrt{2\pi}\int e^{\frac{-1}{2}\left(\frac{x}{\sigma}\right)^2} e^{-k_x x} dx \tag{2}$$

where k_x is the projection of the wavenumber along the X axis and $\beta = k_z$ is the wavenumber corresponding to the propagation direction, see Fig. 5a. First, the plane-waves propagate in free space from the tip to the sample surface (i.e. a typical air gap of 10 nm under feedback conditions, represented by the distance "d" in Fig. 5b). At this point, reflection at the surface (and later at rest of interfaces) is considered according to condition (i) and beneath it, the plane-wave components propagate through an inhomogeneous medium (the sample upper-layer). As an approach, the light transmission can be calculated by an effective medium approximation (condition ii), due to the variations in the refractive index during the light propagation. The transmission of each plane-wave at the sample surface is determined through the boundary conditions of Maxwell equations between two dielectric media (Hecht E. & Zajac, 1997):

$$T_{eff}^{(\beta)} = [t_{eff}^{(\beta)}]^2 = \left| \frac{E_{eff}^{(\beta)}(x, z = d)}{E_i^{(\beta)}(x, z = d)} \right|^2 \tag{3}$$

Let notice that, if a suitable reference plane is chosen for the angular spectrum decomposition, the transmission for each incident plane wave, $E_i(\beta)$, would correspond to the Fresnel coefficient at the incidence angle

$$\theta_i = \text{Arcsin}(kx / n_{air}\, k_0) \tag{4}$$

which is related with the β-wavenumber by

$$\beta_i^2 = n_{air}\, k_0^2 - k_x^2 \tag{5}$$

while the angle of the transmitted wave can be directly obtained from the Snell's law (Hecht E. & Zajac, 1997)

$$\theta_{eff} = Arc\sin\left[\frac{n_{air}}{n_{eff}} \sin\theta_i \right] \tag{6}$$

Once the light traverses the upper-layer it suffers a second reflection (and refraction) at the interface with the homogeneous refractive index material. Expressions like (3)-(6) can be deduced again to determine the transmission coefficients through the second layer, but, in this case, the incidence angle corresponds to the inclination of waves in the effective media (θ_{eff}),

$$T_{sl}^{(\beta)} = [t_{sl}^{(\beta)}]^2 = \left| \frac{E_{sl}^{(\beta)}(x, z = d + 2\lambda)}{E_{eff}^{(\beta)}(x, z = d + 2\lambda)} \right|^2 \tag{7}$$

Before reaching the photodetector in transmission configuration, the light arrives at the substrate-air interface which introduces a last transmission coefficient:

$$T_{air}^{(\beta)} = [t_{air}^{(\beta)}]^2 = \left| \frac{E_{air}^{(\beta)}(x, z)}{E_{sl}^{(\beta)}(x, z)} \right|^2 \tag{8}$$

Notice that in this interface the plane-waves arriving with an incidence angle larger than the critical one for total internal reflection (θ_{tir}) will not contribute to the optical signal. At the same time, the finite dimensions of the detector must be also taken into account since the numerical aperture (NA) of the photodiode could also introduce another limiting angle. Having both facts into account, it is defined the cut-off wave-number, β_c = NA k_0, like the maximum wave-vector of the propagated light, which is equivalent to a maximum receiving angle θ_c by the relation $\beta_c^2 = n_i\ k_0(1\text{-}\sin 2\theta_{cut})$ (Hecht B. et al., 1998), limited by either the detector or total internal reflections. As a result, the expression for the light arriving to the detector can be written as:

$$T = \sum_{-\beta_c}^{\beta_c} T_{air}^{(\beta)} T_{sl}^{(\beta)} T_{eff}^{(\beta)} \left| c^{(\beta)} \right|^2 \tag{9}$$

It is worth noting that during the wave-front propagation the Gaussian beam coming from the NSOM suffer a great divergence. Therefore, if the upper-layer is extended beyond the near-field (e.g., upper-layer up to 2λ thick) the electromagnetic field distribution at the interface with the second layer is considerably extended. In these conditions the second layer can be considered as a homogeneous media with a constant refractive index, satisfying condition (ii). On one hand, the precision estimating the values for the thickness of layers are not critical for the semi-quantitative discussion aimed in this work since such parameter mainly affects the phase of the propagating fields. Nevertheless, it is necessary to point out that the real thickness of each layer must be had into account in certain cases, like in very thin films (thickness << λ) or stratified media (with possible optical resonances) for which multiple reflections are expected to contribute significantly to the transmitted field. In those cases, it is recommended to calculate the transmission coefficients having into account the phase component (Chilwell & Hodgkinson, 1984; Yeh, Yariv & Hong, 1977). On the other hand, samples which consist of a photonic device (like waveguides, beam splitters, optical filters, amplifiers, etc) would requires the decomposition of the sample profile in multiple layers with the aim to distinguish between the different interfaces delimiting the device geometry. For instance, in Ref. (Canet-Ferrer et al., 2008) we simulated the refractive index contrast produced by solid phases present on the surface of a channel waveguide in lithium niobate. In that case, the presence of the waveguide was considered by introducing an additional layer.

3.2 Effective media approach

It is necessary to point out that according to condition (ii) the effective refractive index is going to depend on the upper-layer local composition. Therefore, a different refractive index must be considered at each measuring point (at each pixel of the transmission image). Figure 2(c) illustrates how the local refractive index could be estimated in a general case. It is based on the effective medium theory (EMT), which during last years has been successfully applied to ferroelectric materials (Sherman et al., 2006). The effective dielectric constant ε_{eff} (and therefore the refractive index) for a N-dimensional material (in our case we limit the model to N=2) comprising inclusions of other material with permittivity ε′ and a filling factor p with respect to the host medium (in our case the upper-layer) with a permittivity ε_{up} is given by (Bruggeman, 1935):

$$\varepsilon_{eff} = \frac{1}{2(D-1)}\{(Dp-1)\varepsilon' + (D-1-Dp)\varepsilon_{up} + \sqrt{[(Dp-1)\varepsilon' + (D-1-Dp)\varepsilon_{up}]^2 + 4(D-1)\varepsilon'\varepsilon_{up}}\} \quad (10)$$

At each pixel we consider the area corresponding to the light cone cross-section limited by the detector and, consequently, the filling factor is determined with respect to such area, as indicated in figure 2c (i.e. the isosceles triangle determined by β_c). As a result, the estimation of the refractive index when scanning the surface of the upper layer by the NSOM tip is based on the convolution between the propagating light cone and the objects producing optical contrast. Assuming that both the hidden object and the host matrix are homogeneous, the effective refractive index profile becomes proportional to the spatial convolution along the scan direction of the cone of light and the scatter depicted in Fig. 5c. Therefore the optical contrast can be directly interpreted by means of geometrical considerations (Canet-Ferrer et al., 2008). Unfortunately, dielectric profile usually presents a Gaussian shape at the ferroelectric domain walls and consequently the effective dielectric constant cannot be determined by means of Eq. 10. In that case the refractive index at the upper layer pixels must be evaluated by means of

$$\varepsilon_{eff} = \frac{\int_S \varepsilon(x,z)dxdy}{\int_S dxdy} \quad (11)$$

Where ε(x,z) represents the dielectric constant as a function of the position and S is the surface defined by the light cone. Eq. 11 can be easily evaluated for the scanning situation depicted in Fig. 6. But in this case the index profile is not a bivaluated function; therefore the effective refractive index and the optical contrast would not be directly related by the respective spatial convolution. Having this fact into account, in the next section we are going to propose and alternative way to extract information from transmission images.

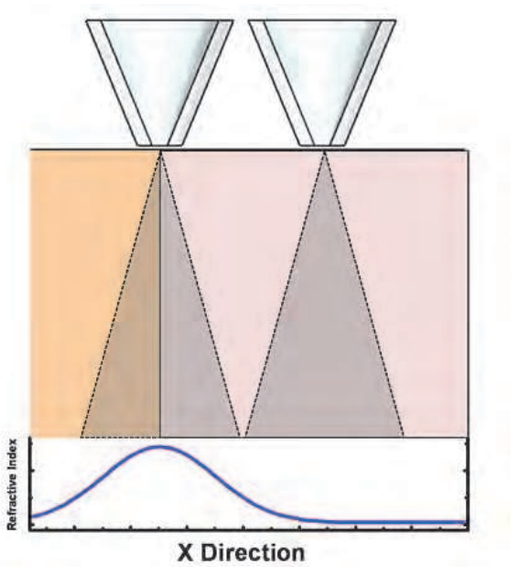

Fig. 6. At the top, it is depicted the NSOM tip in two different points: i) the domain wall and ii) the center of a wide ferroelectic domain. It is also marked the evaluation area as shadowed triangles. At the bottom, the refractive index profile is represented.

4. Characterization of the domain walls in potassium niobate.

In this section we are going to study the refractive index profile induced by ferroelectric domains in a potassium niobate ($KNbO_3$) bulk sample performed by means of NSOM. The potassium niobate $KNbO_3$ (KNO) belongs to the group of perovskite-type ferroelectric materials, like the Barium Titanate. At room temperature, the KNO has an orthorhombic crystal structure with space group Amm_2 and presents natural periodic ferroelectric domains with 180^o spontaneous polarization (Topolov, 2003). Extensive theoretical and experimental studies have been performed on this material since the discovery of its ferroelectricity (Matthias, 1949), due to its outstanding electro-optical, non-linear optical and photorefractive properties (Duan et al., 2001; King-Smith & Vanderbilt, 1994 ; Postnikov et al., 1993; Zonik et al., 1993). In the last decade, the KNO has received much attention due to the relation existing between the piezoelectric properties and the domain structures. However, many of these properties are not well understood at the nanometer scale. From the technological point of view some ferroelectric crystals, as KNO, form natural periodic and quasi-periodic domain structures. The motion of such domain wall plays a key role in the macroscopic response. For this reason, a variety of experimental techniques such as polarizing optical microscopy, anomalous dispersion of X-rays, Atomic Force Microscopy (AFM), Scanning Electron Microscopy (SEM) and Transmission Electron Microscopy (TEM), have been used to study the electrostatic properties of the KNO domains (Bluhm, Schwarz & Wiesendanger, 1998; Luthi et al., 1993; Yang et al., 1999). From the different techniques employed in the domain structure characterization, the Electrostatic Force Microscopy (EFM) and Piezoelectric Force Microscopy (PFM) have been turned into useful practices (Labardi, Likodimos & Allegrini, 2000), since such techniques are based in the electrostatic interaction between the AFM tip and the surface polarization. But unfortunately both methods present important limitations working with bulk materials due the huge external electric field required for inducing the mentioned interaction. As an alternative, the NSOM has been used to demonstrate how the optical characterization of the ferroelectric domains is able to offer useful information even working with bulk materials.

The advantage of our NSOM consists of the possibility of acquiring the images with nanometric resolution, containing the optical information and the topographical features, simultaneously. In the present sample, our probes reached a resolution better than 100 nm on the lateral directions and around 1-3 nm in height (in topography). About the optical images, it can be distinguished two main components contributing to the near-field signal: i) surface scattering and ii) evanescent waves transformed in propagating waves in the presence of a refractive index enhancement (Wang & Siqueiros, 1999). In the first case, the scattering is more important as the light source is closer to the surface; thus scattered waves mainly contain information about the interaction of the tip with the surface roughness. On the other hand, information of the local refractive index (effective refractive index estimated by means of Eq. 11 for the upper layer) is manly contained in the evanescent waves arriving to the detector. Depending on the ratio between both contributions the transmission signal could contain topographical features merged with the optical contrasts (Hecht et al., 1997).

In a previous work the scattering contribution was demonstrated to be considerably reduced by using a visible light source as excitation (Canet-Ferrer et al., 2007). In addition, the topography contribution can be even negligible in KNO due to the huge refractive index

contrast in this material. For example, Fig. 7 shows two NSOM images (topography and transmission) acquired simultaneously. The topography image (Fig. 7a) shows a certain roughness forming elongated structures with a depth of around 5-7 nm (Fig. 7b) that we attribute to the sample polishing process. In contrast, the transmission image (Fig. 7c) is mainly composed by wider optical modulations (Fig. 7d) orientated on a different direction (with respect to surface features), and thus the optical contrasts cannot be correlated with topography details. For a better comparison, the profiles extracted from Figs. 7a and 7c (marked with a grey line) are depicted in Figs. 7b and 7d. It can be changes in the transmitted light larger than 30-35 mV over an average absolute value for the transmission intensity around 2 V. Assuming that the observed optical modulations are produced by the refractive index contrast at the domain walls, the resulting optical contrast would be in the order of predictions and measurements in pervoskite-type materials (Otto et al., 2004; Chaib, Otto & Eng, 2002a; Chaib et al., 2002b).

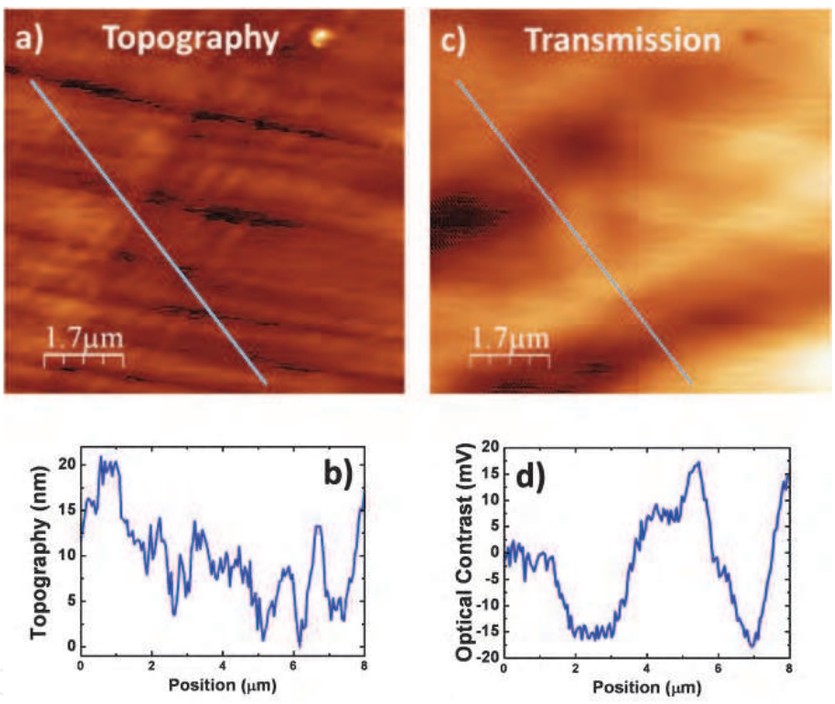

Fig. 7. Topography image (a) and profile along the blue line (b) of a KNO surface. Idem for transmission image in (c) and (d).

The next step consists of deducing a relation between the measured optical contrast and the refractive index. On the one hand, close to the domain wall the effective dielectric constant at the upper-layer is better estimated by means of Eq. 11. On the other hand, the relation between the optical contrast and the effective refractive index is rather complicate. For this reason, it would be more helpful to establish simple relations between the refractive index and the transmission of plane waves composing the Gaussian excitation beam. For example, the optical contrast ($\Delta T^{(0)}$) produced by the normal incidence component ($\beta=0$) as a function of the refractive index change in different points of the upper layer (Δn) can be expressed as follows:

$$\frac{\Delta T^{(0)}}{T^{(0)}} = -\frac{(n-1)}{n+1}\frac{\Delta n}{n} \tag{12}$$

being $T^{(0)}$ the transmittance of the mentioned plane wave and n the refractive index of the material at the point of incidence. However, not all the plane waves in the angle range defined by $[-\beta_c, \beta_c]$ will contribute to the optical contrast with the same intensity. In fact, almost 85% of the electromagnetic field intensity is contained at the low inclination waves, being the normal incidence ($\beta=0$) the main amplitude component. In order to illustrate this fact, in Fig. 8 it is shown the transmittance of a material (with refractive index 2.2 at the second layer) as a function of the upper-layer effective refractive index. The calculation is performed by considering that transmitted light is measured through an extended detector (high NA), which means that β_c is limited by θ_{tir}. Calculated curves stand for the entire Gaussian excitation field (red line) and for only the contribution of normal incidence plane wave (blue line). As above suggested, the transmittance of the electromagnetic field distribution is noticeably influenced by the normal incidence component. It is also worth mentioning that the transmittance change can be approximated by a linear behaviour for relatively small index contrast, being the slope of both curves quite similar in such case. Consequently, even if the approximation of a point-like light source by a planar wave could seem rough, very close values of ($\Delta T/\Delta n$) are expected in both cases.

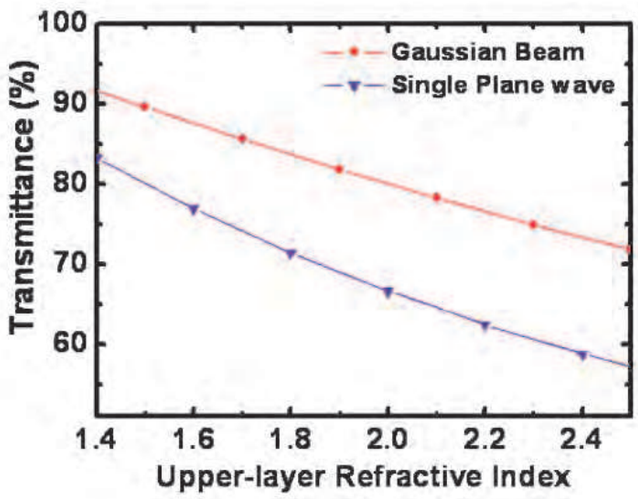

Fig. 8. Transmittance calculated the entire Gaussian beam (red line) and its normal incidence component (blue line) through a two layer sample as a function of the upper-layer effective refractive index. The thickness of each layer is selected according to the real KNO sample dimensions: 2λ for the upper-layer, 1mm for the second layer.

Thanks to this fact, transmission images can be converted into refractive index images by means of a simple expression:

$$\frac{\Delta T}{T} \cong \frac{\Delta T^{(0)}}{T^{(0)}} = -\frac{(n-1)}{n+1}\frac{\Delta n}{n} \tag{13}$$

where now T is the averaged optical signal of a transmission image and ΔT is the experimental optical contrast between two different pixels. The details of the calculation (normalization, numerical aperture effects, tip-sample distances, etc) and its limitations (related with the domain size) are out of the scope of the present work. However, Eq. 13 represents a very simple and semi-quantitative expression to account for local refractive index contrasts in a given material, applicable if the component β=0 dominates the transmittance. As an example, Fig. 9a shows a transmission image acquired under similar conditions to Fig. 7b, but in another zone of the sample. From Fig. 9a we generate the corresponding refractive index image (Fig. 9b) by applying Eq. 13. We can associate optical variations of around 14 mV (with respect to an average background signal of 2V) with refractive index contrasts of around 3% (with respect to the KNO bulk refractive index n_{sl}= 2.2) by comparing a given profile line in both images (Figs. 9c and 9d). Quantitatively, such a contrast is large as compared to reported values in other ferroelectric materials (Canet-Ferrer et al., 2006; Lamela et al., 2009; Han et al., 2009). On the other hand, it is in agreement with respect to the theoretical predictions in Ref. (Chaib et al., 2002b).

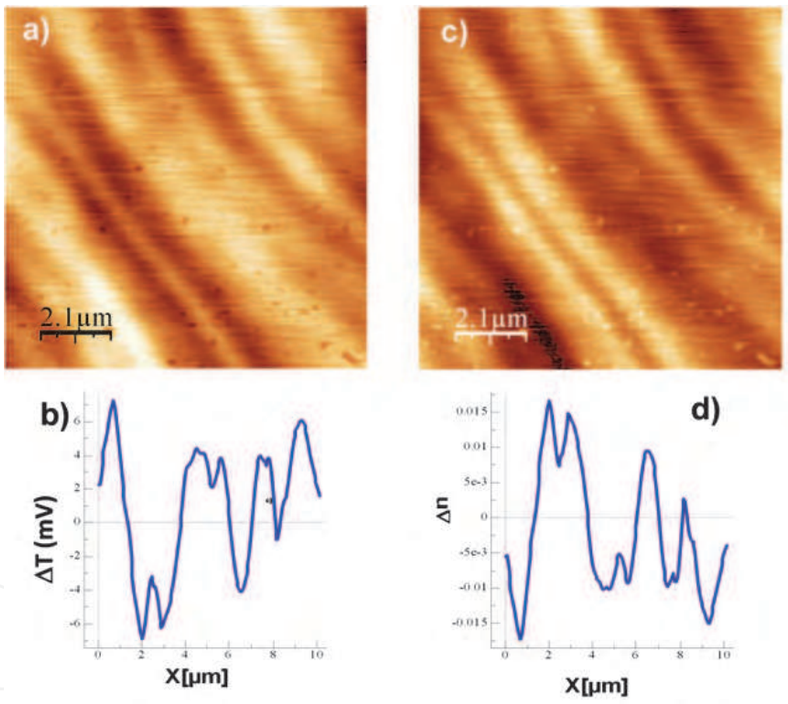

Fig. 9. Transmission (a) and the corresponding refractive index contrast image (c) of the KNO surface. They are accompanied by the corresponding profiles (b) and (d), respectively.

Finally the refractive index images can be used for studying the periodicity and width of the domains by means of averaging the profiles extracted from many images. After comparing several zones of the sample surface, it is observed certain dependence of the optical contrast on the domain width. The results are plotted in Fig. 10a like a scatter cloud where, despite the dispersion in the experimental data, it is observed a clear tendency to increase the refractive index contrast with the size of the domains. A priori this result could seem contradictory, since it is supposed that the larger domains could easily relax the strain at the

interfaces. In fact, Chaib et al. calculated the refractive index contrast for different domain sizes and showing how such contrast become smaller for walls belonging larger domains, contrary to our observations. Consequently we can conclude there is another effect related with the domain size influencing the optical contrast measurement. This effect could be explained attending to the expected refractive index profiles at the domain walls (Fig. 6). For this purpose, the refractive index images have been fitted to Gaussians profiles, one for each domain wall. As a result we can conclude that in our sample the domain walls are not separated enough to observe a fully developed refractive index contrast, as illustrated in Fig. 10b. At the top panel two separated domain walls (red horizontal line) leads to a maximum optical contrast (blue vertical arrow). At the bottom panel of Fig. 10b, the measured contrast (and width) is highly reduced when the domain walls get closer. The optical contrasts are thus underestimated in this case as previously reported (Han et al., 2009).

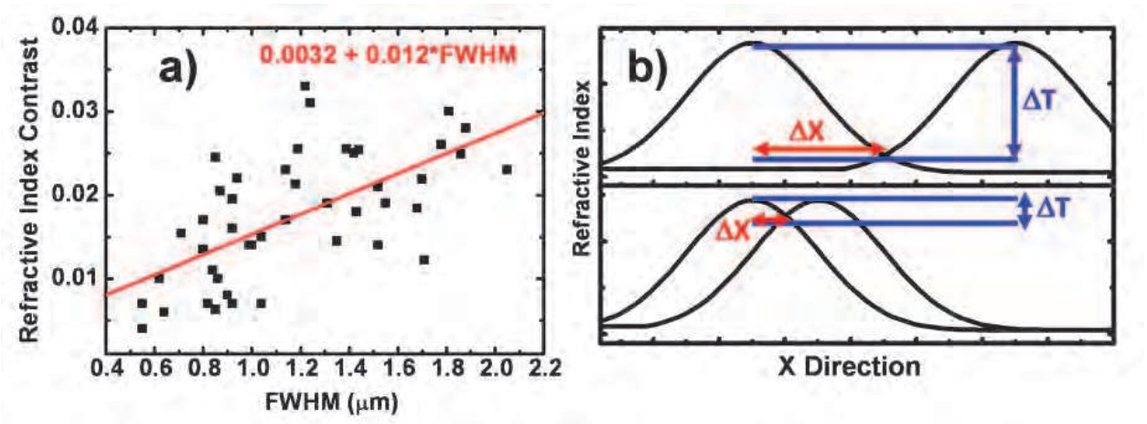

Fig. 10. (a) Optical contrast as a function of the domain size; (b) effect of proximity between the domain walls on the optical contrast.

5. Conclusions

The AFM main properties have been described with the aim to approach the reader to the SPM microscopes. The characteristics of a commercial AFM electronics have been specified since it is the basis of our NSOM. The NSOM illumination configuration has been described in order to study ferroelectric materials. Even if EFM and PFM are the most used techniques to observe electrostatic effects in ferroelectric thin films, NSOM characterization can offer information on the refractive index changes at the domain structure. In the near-field images we observe a clear optical contrast at the domain walls which an average value is around 2% in transmission. These contrasts appear with negligible effect of the topographic features and presenting certain dependence on the separation between domain walls. Thanks to the refractive index contrast images, the average separation between domain walls is found to be around 1.5 μm. Finally, it is worth noting the fact that NSOM imaging provides the possibility of characterizing bulk samples, which are inaccessible by EFM or PFM, without a special preparation of the surface (chemical selective etching, for example), as done to observe periodic domain structures by standard optical microscopy.

6. Acknowledgements

The main author, J. C.-F., thanks the Spanish MCI for his FPI grant BES-2006-12300.

7. References

Abbe E (1882) J. Roy. Micr. Soc. 3 300.

Asenjo A, Jaafar M, Navas D & Vazquez M (2006). *Quantitative magnetic force microscopy analysis of the magnetization process in nanowire arrays.* J. Appl. Phys. 100 023909.

Bluhm H, Schwarz UD & Wiesendanger R, (1998). *Origin of the ferroelectric domain constrast observed in lateral force microscopy.* Phys. Rev. B, 57, 161.

Bruggeman DAG, (1935). "*Berechnung verschiedener physikalischer Konstanten von heterogenen Substanzen*", Ann. Phys. 24 636.

Canet-Ferrer J, Martin-Carron L, Martinez-Pastor J, Valdes JL, (2006). *Scanning probe microscopy applied to the study of domains and domain walls in a ferroelectric $KNbO_3$ crystal.* Bol. Soc. Esp. Ceram y Vidrio, 45, 218.

Canet-Ferrer J, Martin-Carron L, Martinez-Pastor J, Valdes JL, Martínez-Pastor, Carvajal JJ & Diaz F, (2006). *Near-field optical and atomic force microscopy studies of a $RbTiOPO_4$ single crystal with ferroelectric domains.* Bol. Soc. Esp. Ceram y Vidrio, 45, 223.

Canet-Ferrer J, Martin-Carron L, Martinez-Pastor J, Valdes JL, Peña A, Carvajal JJ & Diaz F, (2007). *Scanning prope microscopies applied to the study of the domain wall in a ferroelectric crystal.* J. Microsc. 226, 133.

Canet-Ferrer J, Martinez-Pastor J, Cantelar E, Jaque F, Lamela J, Cussó F & Lifante G (2008). *Near-field scanning optical microscopy to study nanometric structural details of $LiNbO_3$ Zn-diffused channel waveguides,* J. Appl. Phys. 104, 094313.

Cefali E, Patane S, Guciardi PG, Labardi M & Alegrini M (2003). *A versatile multipurpose scanning probe microscope.* J. Microsc. 210 262.

Chaib H, Otto T & Eng LM, *Theoretical study of ferroelectric and optical properties in the 180º ferroelectric domain wall of tetragonal $BaTiO_3$.* Phys. Stat. Sol., 233, 250.

Chaib H, Schlaphof F, Otto T & Eng LM (2002). *Electrical and Optical Properties in 180º Ferroelectric Domain Wall of Tetragonal $KNbO_3$.* Ferroelectrics 291, 143.

Chilwell J &Hodgkinson I, (1984). *Thin-films field transfer matrix-theory of planar multilayer waveguides and reflection from prism-loades waveguides.* J. Opt. Soc. Am. A, 1, 742.

Duan C, Mei WN, Liu J & Hardy JR, (2001). *First-principles study on the optical properties of $KNbO_3$.* J. Phys. : Condens. Matter. 13, 8189.

Eng LM, Guntherodt HJ, Rosenman G Skliar A Oron M, Katz M & Eger D (1998). *Nondestructive imaging and characterization of ferroelectric domains in peridodically poled crystals.* J. Appl. Phys. 83, 5973.

Eng LM (1999). *Nanoscale domain engineering and characterization of ferroelectric domains.* Nanotechnology, 10, 405.

Eng LM & Gutherodt HJ, (2000). *Scanning force microscopy and near-field scanning optical microscopy of ferroelectric and ferroelastic domain walls.* Ferroelectrics, 236 35.

Han TPJ, Jaque F, Lamela J, Jaque D, Lifante G, Cusso F & Kamiskii AA (2009). *Effect of the ferroelectric domain walls in the scanning near field optical microscopy response of*

periodically poled $Ba_2NaNb_5O_{15}$ and $LiNbO_3$ crystals. J. Phys.: Condens. Matter. 21, 042201.

Hecht B, Bielefeldt H, Novotny L, Heinzelmann H & Pohl DW, (1997). *Facts and artefacts in near-field optical microscopy.* J. Appl. Phys. 81, 2492.

Hecht B, Bielefeldt H, Novotny L, Heinzelmann H & Pohl DW, (1998). *Influence of detection optics on near-field optical imaging,* J. Appl. Phys. 84 5873.

Hecht E & Zajac A (1997). *Optics,* ISBN 978-0805385663-5, 3rd ed., Addison Wesley, Reading, M A, Boston.

Hell S & Stelzer E.H.K. (1992). *Properties of a 4Pi confocal fluorescence microscope.* J. Opt. Soc. Am. A, 9 2159.

Harke B, Keller J, Ullal C.K. Westphal V Schoenle & Hell S (2008). *Resolution scaling in STED microscopy.* Optics Express, 16 4154.

Kawata S, Ohtsu M & Irie M (2000). *Nano-Optics,* ISBN 3-540-41829-6, Springer-Verlag. Berlin/Heidelberg.

King-Smith RD & Vanderbilt D, (1994). *First-principles investigation of ferroelectricity in perovskite compounds*. Phys. Rev B, 49, 5828.

Kwak KJ, Hosokawa T, Yamamoto N, Muramatsu H & Fufihira M (2000). *Near-field fluorescence imaging and simultaneous observation of the surface potential.* J. Microsc. 202 413.

Labardi M, Likodimos V, Allegrini M, (2000). *Force-microscopy contrast mechanisms in ferroelectric domain imaging*. Phys. Rev. B, 61, 14390.

Lamela J, Jaque F, Cantelar E, Jaque D, Kaminskii AA & Lifante G, (2007). *BPM simulation of SNOM measurements of waveguide arrays induced by periodically poles BMM crystals*. Optical and quantum electronics, 39 10.

Lamela J, Sanz-Garcia JA, Cantelar E, Lifante G, Cusso F, Jaque F, Canet-Ferrer J & Martinez-Pastor J (2009). *SNOM study of ferroelectric domains in doped $LiNbO_3$ crystals.* Physics Procedia: 2008 Interantional conference on luminescence and optical spectroscopy of condensed matter, 2, 479.

Lifante G. Lamela J, Cantelar E, Jaque D, Cusso F Zhu SN & Jaque F, (2008). *Periodic ferroelectric domain structures characterization by Scanning Near Field Optical Microscopy.* Ferroelectrics, 363 187.

Luthi R, Haefke H, Meyer KP, Meyer E, Howald L & Guntherodt HJ, (1993). *Surface & domain structures of ferroelectric crystals studies with scanning force microscopy*, J. Appl. Phys. 74, 7471.

Matthias BT, (1949). *New ferroelectric crystals*. Phys. Rev., 75, 1771.

Nieto-Vesperinas M, (2006). *Scattering and diffraction in physical optics,* 978-9812563408-7, (2dn ed.)World Scientific, Singapore

Otto T, Grafström S, Chaib H & Eng LM (2004). *Probing the nanoscale electro-optical properties in ferroelectrics.* Appl. Phys. Lett. 84, 1168.

Paeleser MA & Moyer PJ. (1996). *Near-field optics : Theory, instrumentation and applications,* ISBN 978-0471043119, (1st Ed) John Wiley&Sons inc., USA.

Postnikov AV, Neumann T, Borstel G & Methfessel M, (1993). *Ferroelectric structure of $KNbO_3$ and $KTaO_3$ from first-principles calculations.* Phys. Rev. B, 48, 5910.

Sherman VO, Tagantsev AK, Setter N, Iddles D & Price T, (2006). *Ferroelectric-dielectric tunable composites,* J. Appl. Phys. 99 074104.

Topolov VY, (2003). *Domain wall displacements and piezoelectric activity of $KNbO_3$ single crystals.* J. Phys. : Condens. Matter., 15, 561.

Wang S, Siqueiros JM, (1999). *Influence of the sample-probe coupling on the resolution of transmitted rear-field optical image.* Opt. Lasers Eng. 31, 517.

Yang TJ, Gopalan V, Swart PJ & Mohideen U, (1998). *Direct observation of pinning and bowing of a single ferroelectric domains wall.* Phys. Rev. Lett., 82, 4106.

Yeh P, Yariv A & Hong CS, (1977). *Electromagnetic propagation in periodic stratified media. I. General Theory.* J. Opt. Soc. Am., 67, 423.

Zgonik M, Schlesser R, Biaggio I, Voit E, Tscherry J & Gunter P, (1993). *Materials constants of $KNbO_3$ relevant for electro-and-acousto-optics.* J. Appl. Phys., 74, 1287.

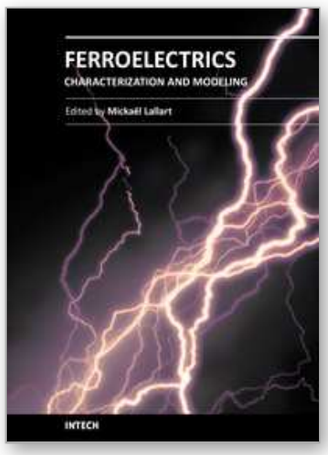

Ferroelectrics - Characterization and Modeling

Edited by Dr. MickaÃ«l Lallart

ISBN 978-953-307-455-9
Hard cover, 586 pages
Publisher InTech
Published online 23, August, 2011
Published in print edition August, 2011

Ferroelectric materials have been and still are widely used in many applications, that have moved from sonar towards breakthrough technologies such as memories or optical devices. This book is a part of a four volume collection (covering material aspects, physical effects, characterization and modeling, and applications) and focuses on the characterization of ferroelectric materials, including structural, electrical and multiphysic aspects, as well as innovative techniques for modeling and predicting the performance of these devices using phenomenological approaches and nonlinear methods. Hence, the aim of this book is to provide an up-to-date review of recent scientific findings and recent advances in the field of ferroelectric system characterization and modeling, allowing a deep understanding of ferroelectricity.

InTech Europe
University Campus STeP Ri
Slavka Krautzeka 83/A
51000 Rijeka, Croatia
Phone: +385 (51) 770 447
Fax: +385 (51) 686 166
www.intechopen.com

InTech China
Unit 405, Office Block, Hotel Equatorial Shanghai
No.65, Yan An Road (West), Shanghai, 200040, China
中国上海市延安西路65号上海国际贵都大饭店办公楼405单元
Phone: +86-21-62489820
Fax: +86-21-62489821

IntechOpen